

# Kinetic control of surface patterning by laser-induced photochemical deposition in liquid solutions. I. Theoretical developments

Emmanuel Hugonnot and Jean-Pierre Delville\*

*Centre de Physique Moléculaire Optique et Hertzienne, UMR CNRS/Université No.5798, Université Bordeaux I,  
351 Cours de la Libération, F-33405 Talence cedex, France*

(Received 2 December 2003; revised manuscript received 17 February 2004; published 27 May 2004)

We theoretically analyze the real-time formation of holographic grating driven by laser-photochemical deposition in liquid solutions. Considering the one-photon excitation of a two-level system, we present a reaction/diffusion description of the species produced photochemically by the excitation of a continuous laser wave. By assuming that a deposit is heterogeneously nucleated on the substrate when concentration of the reaction product reaches solubility, we develop a thermodynamic analysis of its late-stage growth under laser irradiation. A rate equation is proposed and used to describe the kinetics of three different types of patterning: dot array, periodic line writing, and holographic grating formed by two interfering beams. In each case, the predicted deposit growth laws show the emergence of scaling regimes that give rise to a universal picture of the processes involved, whatever the initial photosensitive medium is. Due to the crucial role played by patterned coatings in numerous practical applications (lithography or holography, for instance), this control *in situ* of the kinetics offers the opportunity to totally monitor the desired patterning. It also suggests the way to develop a unified description for holographic grating formation driven by photochemical deposition.

DOI: 10.1103/PhysRevE.69.051605

PACS number(s): 81.15.Fg, 81.10.Dn, 42.40.Eq, 42.70.Gi

## I. INTRODUCTION

Control over mesoscopic periodic structures or patterns of solid materials is of great interest for the development of functional devices, with applications going from organized micro-reactors and microsensors to optics and photonics [1]. For a few years, aside from conventional [2] and advanced [3] lithographic techniques, or assembling [4] and soft lithography [5] procedures, patterning based on diffusion processes is being promoted because it exhibits many advantages, such as single step writing and smart tailoring over the induced arrangement at the desired mesoscopic length scale. An appealing approach consists in using laser waves to build these patterns. Among the diversity of media used (photopolymers [6], polymer-dispersed liquid crystals [7], or artificial suspensions of nanoparticles/microparticles [8], for instance), those resulting from diffusion-driven phase transitions or surface-directed spinodal decomposition [9] are of particular interest for two main reasons. First, the material becomes intrinsically inhomogeneous after a quench within the miscibility gap, giving birth to growing domains of the minority phase. Then, while the following organization can be tailored by deposition on patterned surfaces that definitively constrains the structure, in laser-induced phase transitions the size of the nucleated domains and their arrangement are monitored in three dimensions by the properties of the light pattern. Classically, these optically induced transitions are driven by laser heating [10], solvent evaporation [11], electrostrictive or thermodiffusive concentration variations [12], or photopolymerization [13]. On the other hand, reaction/diffusion processes also give birth to periodic patterning via Turing instability [14] and Liesegang figures

[15], for instance. In this case, irreversibility comes from the chemical reaction and spatially periodic patterns are driven by diffusion of the reaction product. Photochemically stimulated deposition belongs to this family. The technique uses UV or visible light sources to efficiently break molecular bonds and induce rapid thin film deposition. When driven by laser radiation, patterning by photodeposition combines the advantages of phase transitions triggered by a reaction/diffusion process (here a liquid/solid transition) and laser light, (i.e., strong localization in excitation), spectral selectivity in molecule activation, and ease of manipulation. That is why this technique represents nowadays a well established alternative for direct writing on surfaces without mask-based photolithography [16]. While many reported experiments use thermal decomposition or photolysis [17] under strong laser irradiation to create vapors of elemental atoms or molecules that adsorb in a second step onto a foreign substrate, photochemical deposition from excitation of photosensitive liquid solutions has received an increasingly important attention [18] because it can be applied to a much broader range of precursors (including molecular compounds). Light energy conversion is also stronger (the material density is larger than that of a gas phase), and production is easy because experiments are generally realized in simple homemade tight cells. Consequently, as photoabsorption cross sections are larger than in gas phase, the process generally requires very moderate beam intensities and thermal decomposition is often prevented. This flexibility [19] offers the opportunity to deposit a large variety of materials going from noble metals [20], semiconductors [21], or dielectrics [22] to bioorganic materials [23]. Moreover, by irradiating liquid solutions with a well-defined light intensity distribution it is possible to write in one step and contactless conditions various types of patterns (such as dot [24] or line [25] assemblies, or more structured architectures such as holographic gratings [26])

\*Email address: jp.delville@cpmoh.u-bordeaux1.fr

onto a flat [27] or a curved [28] solid substrate in contact with the photosensitive solution. Laser light behaves as an optical pencil which can tailor the material deposition in a very “smart” manner by simply modifying the wavelength used, the intensity distribution, and its spatial extension.

Although the basic principles of photodeposition are rather simple, any particular application requires to carefully tailor the properties of the material deposited. However, photodeposition involves the kinetics of a liquid/solid phase transition under an external field, here an optical excitation. While the dynamic coupling between phase transition and ordering makes this morphogenesis problem rich and challenging, it also implies that control over these nonequilibrium processes is a difficult task, not only because the deposit growth needs to be tailored but also because metastability is a key phenomenon of first-order phase transitions. A thermodynamic description of the kinetics of deposition under laser exposition is then crucial to predict the performances of the final devices since they strongly depend on the size, shape, and distribution of these deposits. Understanding of these various phenomena is nevertheless at an early stage [15] because their theoretical treatment involves subtle couplings between photochemically stimulated reaction/diffusion systems and coarsening by diffusion/adsorption within properly fashioned inhomogeneous electromagnetic field.

The present study is devoted to the analysis of these couplings. We theoretically describe the kinetics of surface patterning by photochemical deposition driven by a continuous laser wave in a reactive solution; confrontation of our model to experiments is presented in a companion paper [29], referred to from now on as Part II. Starting from a reaction/diffusion scheme involving the one-photon excitation of a two-level system, we describe the thermodynamic behavior of the field variation of the photoreaction product. Assuming a low solubility onset of the produced species (a condition required in any efficient deposition process) and considering that growth is driven by a solute adsorption mechanism, we deduce the coarsening of the resulting deposit as a function of light intensity distribution. Beyond prediction of photodeposit growth itself, our goal here is to understand how these kinetic aspects can be efficiently used to build large periodic patterns, such as holographic gratings, and tailor their optical properties in terms of phase and amplitude objects. Indeed, different sort of periodic structures can be created. Dot or line arrays are generally realized according to a serial procedure; they are built element by element. As control over the entire pattern means that each element should be identical to each other in both radial extension and height, this strategy requires great efforts directed towards the growth of a single elemental brick to ensure reliable duplication. On the other hand, parallel procedures are usually implemented by using the fringe pattern of several interfering pump beams. In this case, the radial periodicity is forced by optical excitation while the important quantity to be tailored becomes the height of the deposit, generally constituted by two superimposed contributions, a modulation over a pedestal. As any particular application requires all these controls, we reconsider these three procedures and predict the growth of dots, lines, and periodic modulations as a function of the exciting

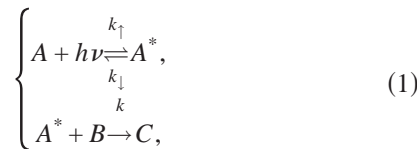
parameters to anticipate the properties of the resulting patterning. Moreover, theories about coarsening [30] show that growth phenomena are described by simple power laws, and hence a scaled dynamics is quite common. Here, we extend this scheme to laser-assisted photochemical deposition. We demonstrate scaling behaviors and explain the origin of these scalings within the general framework of coarsening theories driven by solute diffusion and mass adsorption. Such an approach is not only of particular interest for fundamental purpose but it has also important drawbacks toward very practical situations since it gives a unified view of photodeposition driven by a one-photon absorption, whatever the photosensitive mixture used is.

The paper is organized as follows. Within the framework of reaction/diffusion processes, we present in Sec. II the fundamental processes at the origin of the photochemical production of a new species from a photosensitive mixture. We also illustrate how this production can easily lead to photodeposition when concentration reaches solubility. Our purpose is illustrated with experimental results presented and quantitatively analyzed in Part II of the series. The growth of a circular deposit is analyzed in Sec. III. We first describe the thermodynamic behaviors of the produced species. Then, we develop a growth model of the deposit based on solute adsorption, including both radial and height growths. We illustrate the different growth regimes that can be observed depending on the interplay between the optically active properties of the initial solution and those of the deposit and the exciting beam characteristics. Emphasis is also directed towards a scaling description of the behaviors predicted. These predictions are extended in Sec. IV to line writing by considering excitation with a scanning beam. The main purpose here is to analyze the influence of the scanning velocity on the transverse line growth under illumination. Using the same formalism, Sec. V is entirely devoted to the growth of surface relief gratings monitored by two interfering pump beams. While most of the existing theories are based on thin sine profiles, we present here a full description of the deposition process, and show then in which conditions these postulated sine profiles are acceptable. We finally conclude in Sec. VI with the opportunity offered by the present work to predict the properties of surface relief gratings driven by one-photon excitation and probe the pertinence of models in view of the experiments presented in Part II of the series.

## II. PHOTOCHEMICAL REACTION AND DEPOSITION FROM LIQUID SOLUTIONS

### A. Variations in concentration driven by a one-photon absorption photochemical reaction

Let us consider a stable liquid mixture composed of two species  $A$  and  $B$  solubilized in an inert solvent. In the presence of continuous laser radiation, we assume that (i) the species  $A$  is light activated at the wavelength used and (ii) only activated  $A$  (denoted  $A^*$  in the following) reacts with the species  $B$  to irreversibly give birth to a product  $C$ . This two-step reaction scheme can be represented as



where  $k_{\uparrow}$ ,  $k_{\downarrow}$ , and  $k$  are the different reaction rates. Assuming that the species  $C$  has a very low solubility, these equations represent the starting point of photodeposition based on the simplest reaction-diffusion process that can lead to photo-

deposition. Note that the reverse reaction  $C \xrightarrow{k_C} A^* + B$  can easily be considered [22], but as soon as we deal with surface patterning by photodeposition, we require a reaction rate  $k_C$  as small as possible to preserve the induced pattern; we thus assume in the following  $k_C \approx 0$ . On the other hand, except for special cases involving forbidden transitions, the kinetics of excitation/relaxation  $A + h\nu \rightleftharpoons A^*$  is generally much faster than any molecular diffusion process involved in the mixture. Then, the concentrations  $N_A$  in  $A$  and  $N_{A^*}$  in  $A^*$ , expressed in number of particles per unit volume, can be estimated independently of the second step of the reaction ( $A^* + B \rightarrow C$ ) and at steady state. This adiabatic approximation simply means that the production of the species  $C$ , which is at the origin of photochemical deposition, is obviously the slowest step of the reaction. In these conditions,  $N_A$  and  $N_{A^*}$  are simply related by  $N_{A^*} = (k_{\uparrow}/k_{\downarrow})N_A$ . To calculate the ratio  $k_{\uparrow}/k_{\downarrow}$ , we suppose that  $A + h\nu \rightleftharpoons A^*$  is governed by the most common situation consisting in a one-photon electronic transition. Then, using the standard Einstein coefficients for the one-photon absorption, and the spontaneous and stimulated emissions [31], we find  $k_{\uparrow}/k_{\downarrow} = I/(2I_S)/[1 + I/(2I_S)]$  and  $dI/dz = -\sigma_A(N_A - N_{A^*})I$  along the propagation axis  $z$ . Here  $I$  is the intensity of the exciting wave, and  $I_S = h\nu/(2\sigma_A\tau^*)$  a saturation intensity related to the lifetime  $\tau^*$  of the excited state  $A^*$  and to the one-photon absorption cross section  $\sigma_A$ . Finally, to avoid any direct or indirect disturbing coupling resulting from saturation effects (self-induced transparency and/or excess overheating, for instance) in the experiments presented in Part II, we will always consider that  $I \ll I_S$ . Solute transport other than diffusion is then eliminated, and the concentration  $N_C$  in  $C$  is described by the following reaction-diffusion equation:

$$\frac{\partial N_C}{\partial t} = D_C \nabla^2 N_C + k N_{A^*} N_B, \quad (2)$$

where  $D_C$  is the mass diffusion constant of the product  $C$ . To work with dimensionless variables and reaction rates expressed in  $s^{-1}$ , we use volume fractions  $\Phi$  instead of concentration  $N$ . We consider the molecular volume  $v_{A^*}$ ,  $v_B$ , and  $v_C$  of particles  $A^*$ ,  $B$ , and  $C$ , and write  $\Phi = vN$ . The resulting reaction rate becomes  $k_{A^*B} = kv_C/(v_{A^*}v_B)$ . On the other hand, in experiments presented in Part II, the area illuminated by the exciting beam is always small compared to the transverse extension of the sample; the medium behaves as a sort of reservoir. We can thus assume that  $\Phi_A \approx \Phi_A^0$  and  $\Phi_B \approx \Phi_B^0$  (i.e., the initial volume fractions in  $A$  and  $B$ ). Working with  $I \ll I_S$ , we obtain

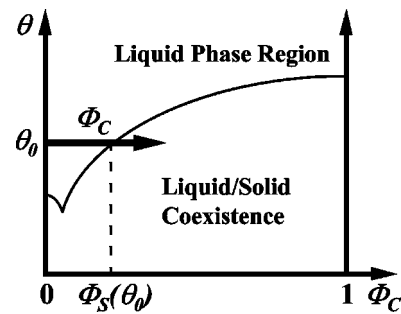


FIG. 1. Schematic concentration/temperature phase diagram of the mixture composed of the initial solution and the species  $C$  produced by the photochemical reaction.  $\Phi_C$  and  $\Phi_S(\theta_0)$  are, respectively, the local concentration in  $C$  generated by laser irradiation and the solubility at the working temperature  $\theta_0$ .

$$\frac{\partial \Phi_C(r, z, t)}{\partial t} = D_C \nabla^2 \Phi_C(r, z, t) + k_{A^*B} \Phi_A^0 \Phi_B^0 \frac{I(r, z)}{2I_S}, \quad (3)$$

where  $r$  represents the radial distance from the beam propagation axis. The first and the second terms of the right-hand side (rhs) of Eq. (3) represent, respectively, diffusion and production of species  $C$ . Since absorbing solutions are always heated by the exciting beam, Eq. (3) should also contain a third term associated to the concentration variation driven by the Soret effect [32]. As this is not the central point of the present work, we neglect here this thermodynamic cross coupling.

### B. Photochemical deposition

According to Eq. (3), production in  $C$  should increase versus light excitation. Then, at a given temperature  $\theta_0$ , nucleation and precipitation occur in the illuminated area as soon as  $\Phi_C$  reaches the solubility  $\Phi_S(\theta_0)$ , as illustrated in the schematic phase diagram presented in Fig. 1. This optical quenching in composition can be used to build surface relief gratings and dynamically control their patterning. Indeed, to illustrate our purpose and show the versatility of the technique, we show in Fig. 2 three examples, taken from Part II, of glass plate patterning by laser-assisted photochemical deposition of chromium hydroxide from a chromate solution. In Fig. 2(a), a periodic structure is realized dot per dot under finite exposition for each deposit followed by a substrate translation perpendicular to the beam axis. On the contrary, if now we let the beam on during a continuous computed displacement of the substrate, stripes are directly written. The grid presented in Fig. 2(b) was realized according to this procedure. Finally, periodic patterning can as well be generated by interfering beams. Figure 2(c) gives an example of such a photodeposited holographic grating.

## III. GROWTH LAW OF A CIRCULAR PHOTODEPOSIT

### A. Photochemical quench in concentration induced by a cw Gaussian beam

To describe how light-induced variation in concentration can drive photodeposition, let us consider that the electro-

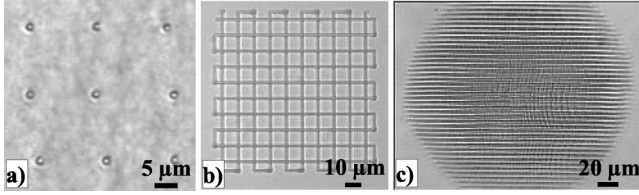


FIG. 2. Holographic gratings generated by laser-assisted photochemical deposition on glass slides in a chromate solution under the excitation of a continuous  $\text{Ar}^+$  laser (wavelength in vacuum  $\lambda_0 = 514$  nm). (a) Dots deposited discontinuously by a serial procedure consisting in a series of finite illumination time followed by a cell displacement; exposition time  $\Delta t = 2$  s, beam waist  $a_0 = 0.9$   $\mu\text{m}$ , and incident beam power  $P = 0.3$  mW. (b) Line array generated under continuous scanning; scanning velocity  $V_S = 5$   $\mu\text{m/s}$ , beam waist  $a_0 = 0.9$   $\mu\text{m}$ , and incident beam power  $P = 0.3$  mW. (c) Holographic grating photodeposited by two interfering pump beams; exposition time  $\Delta t = 20$  s, fringe spacing  $\Lambda_0 = 5$   $\mu\text{m}$ , beam waist  $a_0 = 156$   $\mu\text{m}$ , and total incident beam power  $P = 10$  mW.

magnetic field is a classical continuous  $\text{TEM}_{00}$  Gaussian laser beam propagating vertically along the  $z$  axis. For large beam waist  $a_0$  and thin samples [i.e., for  $l \ll (2\pi a_0^2 n_s)/\lambda_0$  where  $l$  is the sample thickness,  $n_s$  the index of refraction of the solution and  $\lambda_0$  the wavelength in vacuum], the beam intensity has almost a cylindrical symmetry. Therefore, at a radial distance  $r$  from the propagation axis and  $z$  from the entrance of the cell containing the photosensitive mixture, its variation is given by the following expression:

$$I(r, z) = \frac{P}{\pi a_0^2} \exp\left[-\left(\frac{r^2}{a_0^2} + \sigma z\right)\right], \quad (4)$$

where  $P$  and  $\sigma$  are, respectively, the incident power and the optical absorption of the mixture; note that  $\sigma \approx \sigma_A N_A^0$  because  $N_A^* \ll N_A \approx N_A^0$  for  $I \ll I_S$ . Equation (3) is then solved according to standard techniques involved in calculations of laser heating in absorbing media [33]. At first, we use the notation  $K_{AB} = k_A^* N_A^0 \Phi_B^0 / (2\pi I_S)$  and rescale the length (respectively time) variables with the beam radius (respectively mass diffusion time scale over the beam radius) as  $R = r/a_0$ ,  $Z = z/a_0$ , and  $W = \sigma a_0$  (respectively  $T = D_C t/a_0^2$ ). Then, we introduce the Laplace transform  $\tilde{\Phi}(s) = \int_0^\infty \Phi(T) \exp(-sT) dT$  for the rescaled time, and the Fourier-Bessel transform  $\Phi(R) = \int_0^\infty \Phi(Q) J_0(QR) Q dQ$  for the radial variable, considering the cylindrical symmetry of the exciting laser wave;  $J_0(x)$  is the zeroth-order Bessel function and  $Q$  the conjugate mode associated to  $R$ . Since the wave is attenuated within the medium, we seek a special solution of the form

$$\tilde{\Phi}_C^{\text{Spec}}(R, Z, s) = \tilde{\Phi}_C^R(R, s) \exp(-ZW). \quad (5)$$

On the other hand, the homogeneous solution is written in the general form

$$\tilde{\Phi}_C^{\text{Hom}}(R, Z, s) = \int_0^\infty \frac{\sum_{i=1}^2 G_i^{\text{Hom}}(Q, s) \exp[(-1)^i Z \sqrt{Q^2 + s}]}{s + (Q^2 - W^2)} \times J_0(QR) Q dQ, \quad (6)$$

where  $G_{i=1,2}^{\text{Hom}}(Q, s)$  are functions to be determined from the boundary conditions. At first, we consider  $\tilde{\Phi}_C(R, Z \rightarrow \infty, s) = 0$  due to the wave absorption in the medium. We assume here that the attenuation length  $1/\sigma$  is small enough to assimilate the sample with a semi-infinite medium; generalization of the model to finite sample can easily be implemented [34], but is unnecessary here. We deduce  $G_2^{\text{Hom}}(Q, s) = 0$ . Moreover, the rigid boundary condition at the entrance of the sample implies that no axial diffusive flux of  $C$  particle is present at  $Z=0$ . This means  $(\partial \Phi_C / \partial Z)_{Z=0} = 0$ . The complete solution that satisfies these conditions is

$$\begin{aligned} \Phi_C(R, Z, T) = & \frac{K_{AB} P}{2D_C} \int_0^\infty \frac{J_0(QR) \exp(-Q^2/4)}{Q^2 - W^2} \\ & \times \left\{ Q \{1 - \exp[-(Q^2 - W^2)T]\} \exp(-WZ) \right. \\ & + \frac{W}{2} \sum_{i=1}^2 (-1)^i \{ \exp[(-1)^i QZ] \text{erfc}[(-1)^i Q\sqrt{T} \\ & + Z/(2\sqrt{T})] \} - \frac{Q}{2} \exp[-(Q^2 - W^2)T] \sum_{i=1}^2 (-1)^i \{ \\ & \times \exp[(-1)^i WZ] \text{erfc}[(-1)^i W\sqrt{T} \\ & \left. + Z/(2\sqrt{T})] \} \right\} dQ. \quad (7) \end{aligned}$$

To illustrate the variation of  $\Phi_C(R, Z, T)$  versus the different variables, we plot in Fig. 3 the radial stationary solution  $\Phi_C(R, Z=0, T \rightarrow \infty) / \Phi_{\text{Max}}$  at the entrance of the medium, as well as the axial stationary behavior  $\Phi_C(R=0, Z, T \rightarrow \infty) / \Phi_{\text{Max}}$  on beam axis. The temporal behavior  $\Phi_C(R=0, Z=0, T) / \Phi_{\text{Max}}$  at the beam center and the entrance of the medium is illustrated in Fig. 4. In these graphs,  $\Phi_{\text{Max}} = \sqrt{\pi} K_{AB} P / (2D_C W)$  corresponds to the maximum concentration rise  $\Phi_C(R=0, Z=0, \infty)_{W \rightarrow \infty}$  when beam attenuation is very large ( $W \gg 1$ ). Note in Fig. 3 that the radial variation in concentration is much wider than that of the exciting beam. This fact comes from the intrinsic structure of Eq. (3), which is completely analogous to a heat transfer equation. This analogy implies that production of the species  $C$  is dissipative. As a consequence  $\Phi_C(R, Z, T \rightarrow \infty)$  is not only proportional to the local field intensity but also strongly depends on boundary conditions. From the mathematical point of view, this nonlocal variation appears through the “ $1/(Q^2 - W^2)$ ” term within the expression of  $\Phi_C(R, Z, T)$ . The same broadening effect also appears on beam axis.

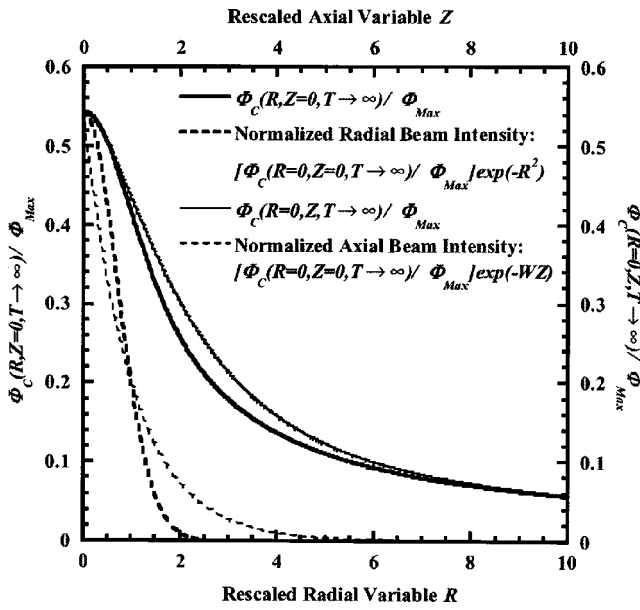


FIG. 3. Radial (respectively axial) behavior of the normalized stationary concentration  $\Phi_C(R,Z=0,T \rightarrow \infty)/\Phi_{Max}$  [respectively  $\Phi_C(R=0,Z,T \rightarrow \infty)/\Phi_{Max}$ ] of the species  $C$  produced photochemically at the entrance of the excited medium (respectively along beam axis) for  $W=1$ . The normalized radial Gaussian shape of the exciting laser beam as well as its axial decay inside the absorbing medium are represented in dashed lines for comparison.  $\Phi_{Max}$  is the maximum concentration rise when the beam attenuation is very large.

### B. Influence of laser-induced heating

Before discussing the domain growth induced by photochemical deposition, we must note that the first observable laser-driven effect is an increase in temperature  $\theta_E$  associated to the light absorbed within the mixture at the wavelength used. The calculation of  $\theta_E$  has already been performed [33]; it is analogous to that developed above for the field-induced variation of the concentration of the species  $C$ . Thus, we just recall here the main results necessary for our purpose. Using the fact that the thermal diffusivity is much larger than the solute diffusion constant  $D_C$ , the overheating is almost instantaneous compared to any concentration variation. In these conditions the temperature rise is calculated in steady state and its largest value is given by

$$\theta_E(R=0,Z=0,W) = \theta_{Max} N(W), \quad (8)$$

where  $\theta_{Max} = \theta_E(R=0,Z=0,W \gg 1) = P/(2\sqrt{\pi}\kappa\alpha_0)$  is the maximum value of the temperature rise and  $\kappa$  is the thermal conductivity of the solution.  $\theta_E$  also depends on a nonlinear function  $N(W)$  of the rescaled absorption  $W$  given by  $N(W) = WD(W/2) - (W/2\sqrt{\pi})\exp(-W^2/4)E_i(W^2/4)$ , where  $D(x) = e^{-x^2} \int_0^x e^{t^2} dt$  and  $E_i(x) = \int_{-\infty}^x (e^t/t) dt$  are, respectively, the Dawson and the exponential Integral functions. Considering the generic phase diagram presented in Fig. 1, the main influence of the temperature variation  $\theta_E$  is to increase the value of the solubility  $\Phi_S$  required to quench the solution without changing any of the mechanisms involved. As we

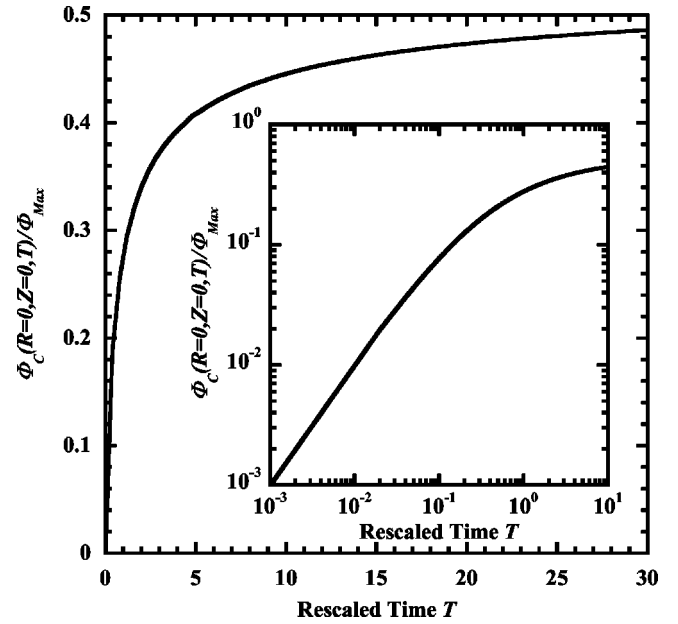


FIG. 4. Temporal behavior of the normalized stationary concentration  $\Phi_C(R=0,Z=0,T)/\Phi_{Max}$  of the species  $C$  produced photochemically at the entrance of the excited medium on beam axis. Inset: log-log plot of the same data to illustrate the early-stage production.  $\Phi_{Max}$  is the maximum concentration rise when the beam attenuation is very large.

have assumed  $I/I_S \ll 1$  in the present model, and thin samples are always used in experiments, we will neglect this second-order effect.

### C. Liquid/solid phase transition induced by a photochemical reaction

The temporal variation presented in Fig. 4 illustrates quantitatively how laser-induced variation in composition can be used to induce a liquid/solid phase transition. Indeed, as  $\Phi_C(R,Z,T) > 0$ , the concentration in  $C$  increases upon laser radiation in the high intensity region. Thus, as already illustrated in Fig. 1, the system is optically quenched in composition when  $\Phi_C(R,Z,T)$  reaches the solubility  $\Phi_S$  at the working temperature. As a result, solid domains constituted by the minority phase (here the species  $C$ ) are nucleated by the field in the solution and grow during further illumination. Since the mixtures used are classically far from criticality, nucleation essentially occurs heterogeneously, either on bulk impurities [35] or substrate defects [30] in the absence of particular treatment. However, substrate defects are generally much larger than bulk impurities present in analytical reagents. The corresponding activation barrier is thus smaller and photodeposition on the substrate is favored. As  $\Phi_C(R,Z,T=0) = 0$ , this also means that a minimum intensity, determined from  $\Phi_C(0,0,\infty) = \Phi_S$ , is necessary to quench the mixture, and that process requires an induction time  $T_{ind}$  given by  $\Phi_C(0,0,T_{ind}) = \Phi_S$ .

### D. Radial growth rate of the deposit

As in any classical experiment the spatial extension of the deposit is always incomparably larger than any molecular

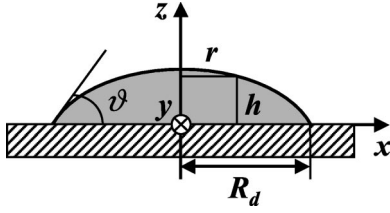


FIG. 5. Shape of the deposit used for the theoretical description of its growth on the substrate. A spherical cap is assumed, where  $R_d$ ,  $h$ , and  $\vartheta$  are, respectively, the radius on the slide, the height, and the contact angle. The deposit growth is described in cylindrical coordinates  $(r, z)$  to take advantage of the laser beam symmetry.

length scale involved in the process, we deal with the so-called late-stage kinetics [36] of the light-induced liquid/solid phase transition. Therefore, we completely neglect the nucleation stage of the transition. We just suppose that a single nucleus is nucleated on the substrate and we assume that its growth results from adsorption of the diffusing  $C$  particles that are photochemically produced in the solution. Moreover, as pure diffusion-limited aggregation would result in a fractal structure [37] which is not observed experimentally (see the textures in Fig. 2) we assume internal reorganization of the adsorbed particles inside the deposit; this early-stage process will be illustrated in Part II. Then, we implicitly incorporate this internal reorganization by considering a “droplet growth” model by diffusion. A sketch of the growth geometry is presented in Fig. 5. The immobile deposit is represented by a spherical cap of height  $h(r, R_d, \vartheta)$  where  $R_d(t)$  denotes its radius on the substrate and  $\vartheta$  the contact angle at the perimeter.  $\vartheta < 90^\circ$  is assumed because efficient photodeposition requires a “wetting” situation. The growth rate of the photodeposit is then obtained by equating its volume change with the normal component of the diffusive flux  $\vec{J}_C = D_C \vec{\nabla} \Phi_C$  over its surface [36]. This leads to

$$\frac{dR_d}{dt} = D_C (\vec{\nabla} \Phi_C \cdot \vec{n})_h, \quad (9)$$

where  $\vec{n}$  is a unit vector perpendicular to the deposit surface. At this stage of the calculation, we should notice that in the previous sections the beam intensity was written as  $I(R, Z) = I_0 e^{-R^2} e^{-WZ}$  while now light will cross the deposit (of normalized height  $H = h/a_0$  and absorption  $W' = \sigma' a_0$ ) before reaching the photosensitive solution; remember that we have assumed a vertical upward beam in agreement with the experiments presented in Part II. Then, we rewrite the beam intensity inside the solution as  $I(R, Z) = I_0 e^{-R^2} e^{-W'Z} e^{-W(Z-H)}$  to take into account light absorption within the deposit. The normal component of the diffusive flux is then obtained by solving the diffusion/reaction equation given by Eq. (3) with the appropriate boundary conditions. At first, we continue to consider  $\Phi_C(R, Z \rightarrow \infty, T) = 0$  due to the wave absorption in the solution. On the other hand, we already supposed that the photodeposit grows by adsorption of the diffusing  $C$  particles at its boundaries. Then, the second boundary condition is

given by  $\Phi_C(R, Z = h/a_0, T) = 0$  at the surface of the deposit. As the radius of the deposit is measured at  $r = R_d$  and  $z = 0$ , we finally find

$$\frac{d\rho_d}{dT} = \cos(\vartheta) \frac{K_{AB} P}{2D_C} \int_0^\infty J_0(Q\rho_d) F(T, Q) \exp(-Q^2/4) Q dQ, \quad (10)$$

where  $\rho_d = R_d/a_0$  is the reduced radius and

$$F(T, Q) = \frac{1}{Q^2 - W^2} \{ -W + Q \operatorname{erf}(Q\sqrt{T}) + W \exp[-(Q^2 - W^2)T] \operatorname{erfc}(W\sqrt{T}) \} \quad (11)$$

is a function that describes the temporal behavior of the diffusive flux normal to the deposit. Note that, contrary to the diffusive mechanisms that govern the kinetics of laser-induced liquid/liquid phase transitions in nonabsorbing liquid mixtures, where the droplet feeding is ensured by the radial mass flux [38], the deposit growth is here totally controlled by the diffusive flux along the beam axis  $D_C (\partial \Phi_C / \partial Z)_H$  because the solute adsorption condition implies  $(\partial \Phi_C / \partial R)_H = 0$ .

While Eq. (10) gives the general expression for the growth rate after the nucleation stage, experiments in phase transition dynamics often deal with the late-stage growth in the adiabatic approximation [39]. In this case, one analyzes growth over period much larger than the mass diffusion time scale and considers that the solute concentration around the growing deposit is almost stationary. According to the temporal behavior of  $\Phi_C(R, Z, T)$ , this approximation operates for  $T > \max\{1, 1/W^2\}$ , i.e., for  $T$  larger than the largest of the radial and the axial diffusion time scales. Consequently, one has  $F(T, Q)|_{\text{adiab}} = 1/(Q + W)$  which yields to

$$\left. \frac{d\rho_d}{dT} \right|_{\text{adiab}} = \cos(\vartheta) \frac{K_{AB} P}{2D_C} \int_0^\infty \frac{J_0(Q\rho_d) \exp(-Q^2/4)}{Q + W} Q dQ. \quad (12)$$

One of the major points of the general theory of coarsening phenomena is a description in terms of scaled dynamics at late stage [30]. We therefore work within this approximation in the following section, and present the different growth regimes that can be predicted from Eq. (12).

### E. Radial growth laws in adiabatic condition

While an efficient photodeposition process requires in any case a reasonably important optical absorption  $\sigma$ , the rescaled absorption  $W$  can nevertheless be made large or small compared to one depending on the beam size. When the beam waist  $a_0$  of the writing beam is close to the diffraction limit, as in the patterning illustrated in Fig. 2(a), we are clearly in the  $W \ll 1$  situation. Then,  $W$  can be neglected in Eq. (12) and the growth rate becomes

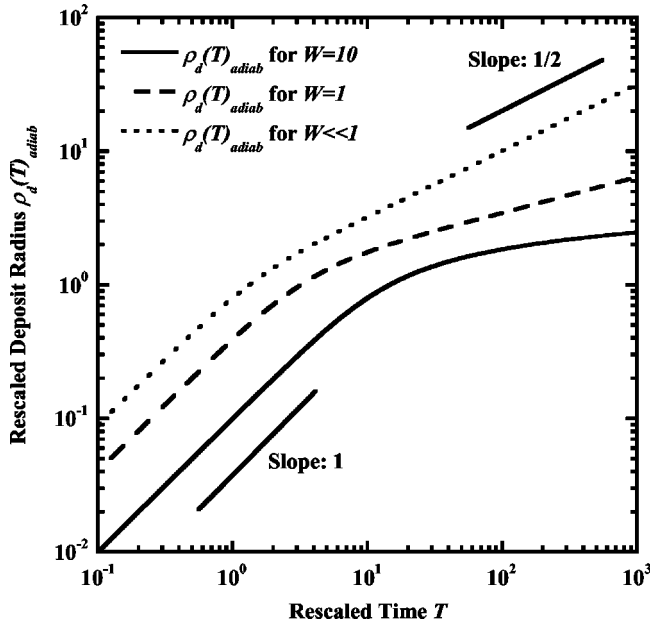


FIG. 6. Normalized late-stage growth of the photodeposit radius in adiabatic conditions in low, intermediate, and high absorption media. The regime  $\rho_d(T)_{adiab} \propto T$  (growth when the Gaussian shape of the beam can be ignored) and the asymptotic late-stage behavior  $\rho_d(T)_{adiab} \propto \sqrt{T}$  at low normalized absorption are depicted. We stated  $\cos(\vartheta)K_{AB}P/D_C=1$  for the comparison.

$$\left. \frac{d\rho_d}{dT} \right|_{W \ll 1} = \cos(\vartheta) \frac{K_{AB}P}{2D_C} \sqrt{\pi} \exp(-\rho_d^2/2) I_0(\rho_d^2/2), \quad (13)$$

where  $I_0$  is the zeroth-order modified Bessel function. If we rescale time by taking  $\tau = \cos(\vartheta)(K_{AB}P/2D_C)\sqrt{\pi}T$ , we see that  $\rho_d(\tau)|_{W \ll 1}$  points out a single-scale dynamics versus optical parameters. Moreover, as  $K_{AB} \propto N_A^0/I_S$  and  $I_S \propto 1/\sigma_A$ , we find that  $K_{AB} \propto \sigma$  and thus,  $\tau$  behaves as  $\tau \propto \sigma(Pt/a_0^2)$ . This means that the kinetics of one-photon photochemical deposition in the  $W \ll 1$  regime is driven by the light energy deposited in the unit interaction volume  $a_0^2/\sigma$ . For  $\rho_d \ll 1$  one has  $\rho_d|_{W \ll 1} \propto \tau$ , which is equivalent in real variables to  $R_d \propto W(Pt/a_0^2)$ . Using the relation  $I_0(x) \approx \exp(x)/\sqrt{2\pi x}$  for  $\rho_d \gg 1$ , we find a second asymptotic behavior  $\rho_d|_{W \ll 1} \propto \sqrt{\tau}$ , which leads to  $R_d \propto \sqrt{\sigma(Pt)}$ . During the late stages of the deposition, i.e., when the deposit radius is much larger than that of excitation, the growth does not feel anymore the influence of the beam waist  $a_0$  and simply depends on the energy deposited in the medium. These behaviors are illustrated in Fig. 6 as well as the variation predicted by Eq. (13) when the initial condition used for integration is  $\rho_d(T=0)|_{W \ll 1} = 0$ .

On the other hand, due to the  $\exp(-Q^2/4)$  term appearing in Eq. (12), the integral contribution for  $Q > 2$  is almost negligible. Consequently, the growth rate in the  $W \gg 1$  regime reduces to

$$\left. \frac{d\rho_d}{dT} \right|_{W \gg 1} = \cos(\vartheta) \frac{K_{AB}P}{D_C W} \exp(-\rho_d^2). \quad (14)$$

We now rescale time by taking  $\tau' = \cos(\vartheta)(K_{AB}P/D_C W)T$ , instead of  $\tau$ , to see that the kinetics still continues to point out a single-scale dynamics. This behavior is nevertheless different from that predicted for  $W \ll 1$ . Indeed, as the new time scale behaves as  $\tau' \propto Pt/a_0^3$ , it is no more dependent on optical absorption. For  $\rho_d \ll 1$ , it is no more dependent on optical absorption. For  $\rho_d \ll 1$ , we find  $\rho_d|_{W \gg 1} \propto \tau'$ , which leads to  $R_d \propto Pt/a_0^2$ . At early stage, growth is simply driven by the light energy per unit surface. This behavior is not surprising because one can assume that  $W \gg 1$  is equivalent to the case of a highly absorbing mixture. Then, only the few first layers of liquid close to the incident substrate feel the beam excitation. The corresponding growth regimes are also illustrated in Fig. 6, as well as the variation predicted by Eq. (14), in order to compare the full set of behaviors predicted by the model. To represent the different growth laws versus  $W$  within the same plot, i.e., with the same reduced variables, we have assumed a constant value of  $\sigma$ , considering that changes in  $W$  are accomplished by modifying  $a_0$ . In addition, we state  $\cos(\vartheta)K_{AB}P/D_C=1$  for the comparison. At first, as deposit growth is driven by the axial concentration gradient, we retrieve the fact that a decrease in  $W$  accelerates its kinetics (see the temporal shift towards larger  $T$  for increasing  $W$  at the early-stage growth). Inversely, the slope of  $\rho_d(T)$  at late stage varies from 1/2 to almost 0 for increasing  $W$  because light is more and more absorbed by the solution.

## F. Thickness of the deposit

If deposits are used in optical systems as phase or amplitude objects [19] or as template for subsequent assembling [40], another important feature is the control over their height because the deposit thickness can strongly affect light transmission properties. Considering our spherical cap model, the height  $h_d$  of the deposit on beam axis is related to its radius  $R_d$  and to the contact angle  $\vartheta$  by the relation  $h_d = [(1 - \cos \vartheta)/\sin \vartheta]R_d$ . Thus, when wetting and surface tension dominate the deposit shape, the temporal behavior of  $h_d$  is simply proportional to the radial growth. Moreover, the proportionality constant  $(1 - \cos \vartheta)/\sin \vartheta$  shows that the better the wetting, the thinner the deposit. Therefore, when both given radial and axial sizes of the deposits are required for a particular application, the substrate should be treated to adjust the contact angle. However, if one can assume that radial growth is controlled by wetting at the edges of the deposit where its height vanishes, such an assumption is much more debatable when dealing with axial growth because the exciting beam is attenuated within the deposit. Consequently, there is no obvious reason to suppose that the shape of large deposits is still controlled by surface tension, particularly close to beam axis where the deposit is the thickest. The preceding determination of  $h_d$  is thus reasonable if and only if deposits are thin and characterized by a weak absorption. If these conditions are not fulfilled, we should take into account the optical absorption of the deposit and remove any forcing driven by surface tension. In this case, we assume that the shape of the deposit is represented by a beam-

centered surface of revolution of height  $h(r)$ . If the curvature of the deposit is weak, i.e.,  $(\partial h/\partial r)^2 \ll 1$ , the height growth rate becomes

$$\frac{dh}{dt} = D_C (\vec{\nabla} \Phi_C \cdot \vec{n})_h. \quad (15)$$

Then, since the height of the deposit is measured at  $r=0$  and  $z=h_d$ , we find

$$\frac{dH_d}{dT} = \frac{K_{AB}P}{2D_C} \exp(-W'H_d) \int_0^\infty F(T,Q) \exp(-Q^2/4) Q dQ, \quad (16)$$

where  $H_d = h_d/a_0$  is the reduced deposit height. Integration of Eq. (16) in the adiabatic approximation, with initial condition  $H_d(T=0)=0$ , leads to

$$H_d = \frac{1}{W'} \ln \left[ 1 + \frac{K_{AB}W'P}{2D_C} \left( \int_0^\infty \frac{\exp(-Q^2/4)}{Q+W} Q dQ \right) T \right]. \quad (17)$$

Even if we choose the beam waist as length of normalization for harmonization purpose, note that Eq. (17) shows that the emerging axial normalization is  $W'H_d = \sigma' h_d$  because the axial length scale is  $1/\sigma'$ . Then, in the presence of highly absorbing media, the growth of the deposit height at beam center is at variance with that predicted from the radial growth when surface tension governs the shape of the deposit: the temporal behavior becomes logarithmic at late stage. Considering as before asymptotic cases, we find that  $\int_0^\infty [\exp(-Q^2/4)/(Q+W)] Q dQ$  equals  $\sqrt{\pi}$  for  $W \ll 1$  and  $2/W$  for  $W \gg 1$ . Then, if we rescale time by  $\tau = (K_{AB}W'P/2D_C\sqrt{\pi}T)$  [respectively  $\tau' = (K_{AB}W'P/D_CW)T$ ] when  $W \ll 1$  (respectively  $W \gg 1$ ), we see that  $W'H_d$  also points out a single-scale dynamics. Moreover, to link these predictions with radial growth behaviors, it can be noticed that  $W'H_d|_{W \ll 1} \propto \tau$  and  $W'H_d|_{W \gg 1} \propto \tau'$  for  $\tau, \tau' \ll 1$ , which are equivalent in real variables to  $h_d|_{W \ll 1} \propto W(Pt/a_0^2)$  and  $h_d|_{W \gg 1} \propto (Pt/a_0^2)$ . Thus, as discussed above, we retrieve the fact that  $h_d$  behaves as  $R_d$  at the early-stage growth (i.e., for thin deposits when their thickness does not influence their growth), but Eq. (17) also demonstrates that deviation irreversibly occurs at larger  $T$ . These behaviors are illustrated in Fig. 7 as well as the general variation predicted by Eq. (17). To represent the different growth laws versus  $W$  within the same plot, i.e., with the same reduced variables, we have assumed  $\sigma' \approx \sigma$ , considering that changes in  $W$  and  $W'$  are monitored by the variation in beam waist  $a_0$ . In addition, we state  $K_{AB}P/D_C=1$  for the comparison. At first, since growth is driven by the axial concentration gradient, we retrieve the fact that a decrease in  $W$  accelerates its kinetics (see the temporal shift towards larger  $T$  for increasing  $W$  at the early-stage growth). Moreover, contrary to radial growth the slope of  $H_d(T)$  at late stage does not vary with  $W$ ; just its amplitude is affected by the absorptions of both the deposit and the photosensitive solution.

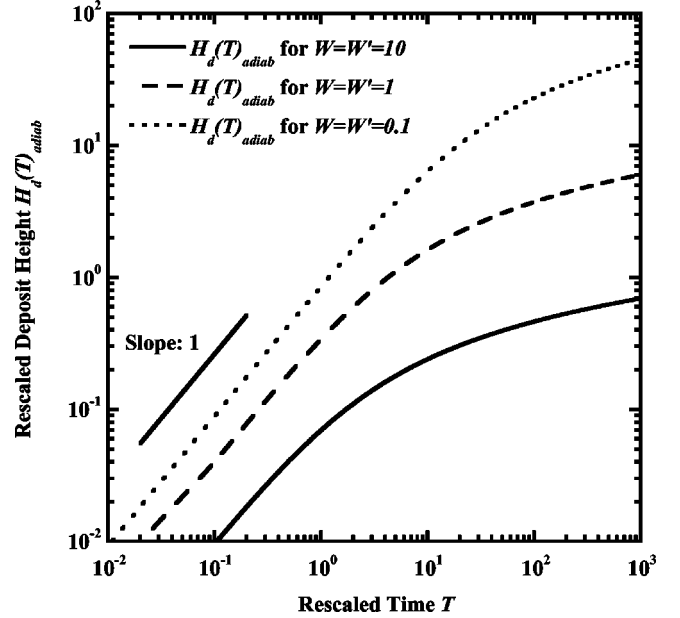


FIG. 7. Normalized late-stage growth of the photodeposit height in adiabatic conditions in low, intermediate, and high absorption media. Note that the deposit height behaves in time and amplitude as its radius (see Fig. 6) at the early growth stage. We assumed  $W = W'$  and stated  $K_{AB}P/D_C=1$  for the comparison.

Finally, note that Eq. (17) is also known as the Elovich growth equation [18], and has already been empirically used by Peled *et al.* [41] to experimentally characterize, with reasonable success, the growth of thin amorphous selenium film photodeposited from colloidal solutions under continuous laser excitation.

#### IV. APPLICATION TO CONTINUOUS WRITING ON SURFACE

While in the preceding section the exciting beam was left stationary, a simple and important extension of the model consists in describing the effect of a scanning beam in order to write lines on the substrate instead of dots. Indeed, in numerous applications, the laser beam is used to generate interconnects [42], to repair circuit defects in microelectronics [43], or to create continuous microscale patterning on surfaces [17,25] as an alternative to conventional lithography. An example of such a surface patterning is presented in Fig. 2(b). In the present section, we thus discuss the influence of the scanning velocity on the size of the lines deposited. As the most appealing practical situation concerns the deposition of narrow lines, we assume in the following that the beam waist of the writing beam satisfies the condition  $W \ll 1$ . Moreover, if  $V_S$  denotes the beam scanning velocity, the normalized characteristic time of deposition is now given by  $T_S = D_C t_S / a_0^2$ , where  $t_S = 2a_0 / V_S$  corresponds to the time required to scan a distance equal to a beam diameter. For reasonable scanning velocities, say  $V_S$  of the order of a few microns per second, one has  $T_S \ll 1$  and deposition during  $T_S$

is described by the early-stage growth regime. One should therefore take into account the time dependence of  $F(T, Q)$  in the growth rate equation [Eq. (10)]. As  $F(T, Q) \approx (2/\sqrt{\pi})\sqrt{T}$ , the line radius behavior obtained for the most

$T \ll 1$  interesting narrow line case is

$$\rho_S \approx \cos(\vartheta) K_{AB} \frac{8\sqrt{2}}{3\sqrt{\pi}} \sqrt{D_C} \frac{P}{(a_0 V_S)^{3/2}}, \quad (18)$$

which shows that  $\rho_S = \rho_d(T=T_S) \propto P T_S^{3/2} \propto P/(a_0 V_S)^{3/2}$ . Consequently, if the beam waist  $a_0$  is held constant as in most experiments, the wideness of the written line can be controlled in a very smart way because it is dynamically monitored by two independent parameters, i.e., either  $P$  or  $V_S$ , depending on the experimental conditions. For highly absorbing liquid mixtures it is preferable to choose low laser power excitations to prevent any alteration induced by thermal decomposition and adjust the amplitude of the scanning velocity, while in the opposite case variations in  $P$  are much more easy to manage if required.

## V. GROWTH OF A SURFACE RELIEF GRATING

In the preceding sections, we focused our attention onto the growth of photodeposited patches and lines, considered as elements of a larger structure. Periodic patterns are thus generated via a serial procedure. Such a strategy, even necessary in some specific situations, is time consuming because patterning is build brick by brick. Deposition of surface relief gratings by interfering pump beams circumvents this problem because a parallel strategy is implemented.

### A. Quench in concentration induced by two interfering beams

To build surface relief gratings, we consider two linearly polarized cw TEM<sub>00</sub> Gaussian lasers of same intensity that interfere on the substrate with an angle  $\psi$ . Thus, three wave vector distributions of width  $2/a_0$  are excited in the medium;  $a_0$  is the waist at beam intersection.  $\Lambda_0 = \lambda_M/[2 \sin(\psi/2)]$ , where  $\lambda_M$  is the laser wavelength in the medium, denotes the resulting fringe spacing and  $q_0 = |\vec{q}_0| = 2\pi/\Lambda_0$ ; these three distributions are, respectively, centered on the wave vectors  $\vec{q} = \vec{0}$ ,  $\vec{q} = \vec{q}_0 = \vec{k}_2 - \vec{k}_1$ , and  $\vec{q} = -\vec{q}_0 = \vec{k}_1 - \vec{k}_2$ ;  $\vec{k}_1$  and  $\vec{k}_2$  are the wave vectors associated to the pumps. The distribution centered around  $\vec{q} = \vec{0}$  (denoted  $q=0$  in the following) represents the contribution of the Gaussian intensity shape of the pumps while those centered around  $\vec{q}_0$  and  $-\vec{q}_0$  (denoted  $q=q_0$  in the following) describe the modulation  $\Lambda_0$  of the fringe pattern. Assuming  $q_0 a_0 \gg 1$  to use the plane wave approximation close to the beam crossing, we write the exciting intensity in the liquid phase as

$$I(X, Z) = \frac{P}{\pi a_0^2} [1 + \cos(Q_0 X)] \exp(-WZ), \quad (19)$$

where  $Q_0 = q_0 a_0$  and  $X = x/a_0$ , represent, respectively the rescaled wave vector and variable along the direction of the modulation. We choose to write  $I_0$  as  $I_0 = [P/(\pi a_0^2)]$  to express the fact that  $P$  continues to represent the total power

injected in the medium. Then, we reiterate the procedure described in Sec. III B to determine the variation in concentration driven by a one-photon absorption photochemical reaction, except that now the spatial decomposition over Fourier-Bessel modes is replaced by the spatial Fourier transform  $\Phi(X) = (1/2\pi) \int_{-\infty}^{+\infty} \Phi(Q) \exp(-iQX) dQ$  due to the plane wave excitation assumption. In these conditions, we find

$$\tilde{\Phi}_C^{Spec}(X, Z, s) = \frac{1}{2\pi} \frac{K_{AB} P}{D_C} e^{-WZ} \int_{-\infty}^{+\infty} \frac{f(Q)}{s[s + (Q^2 - W^2)]} e^{-iQX} dQ, \quad (20)$$

where  $f(Q) = \int_{-\infty}^{+\infty} [1 + \cos(Q_0 X)] e^{iQX} dX = 2\pi [\delta(Q) + 1/2 \delta(Q - Q_0) + 1/2 \delta(Q + Q_0)]$  represents the optical excitation in Fourier space and  $\delta(x)$  is the Dirac distribution. On the other hand, the homogeneous solution of Eq. (3) is written in the general form:

$$\tilde{\Phi}_C^{Hom}(X, Z, s) = \frac{1}{2\pi} \int_{-\infty}^{+\infty} \frac{\sum_{i=1}^2 G_i^{Hom}(Q, s) \exp[(-1)^i Z \sqrt{Q^2 + s}]}{s + (Q^2 - W^2)} \times e^{-iQX} dQ. \quad (21)$$

Considering  $\Phi_C(X, Z \rightarrow \infty, T) = 0$  and rigid boundary conditions at the entrance of the sample [ $(\partial \Phi_C / \partial Z)_{Z=0} = 0$ ], the complete solution for  $\Phi_C(X, Z, T)$  is

$$\begin{aligned} \Phi_C(X, Z, T) = & \frac{1}{2\pi} \frac{K_{AB} P}{D_C} \int_{-\infty}^{+\infty} \frac{f(Q) e^{-iQX}}{Q(Q^2 - W^2)} \\ & \times \left( Q \{1 - \exp[-(Q^2 - W^2)T]\} \exp(-WZ) \right. \\ & + \frac{W}{2} \sum_{i=1}^2 (-1)^i \{ \exp[(-1)^i QZ] \operatorname{erfc}[(-1)^i Q\sqrt{T} \\ & + Z/(2\sqrt{T})] \} - \frac{Q}{2} \exp[-(Q^2 - W^2)T] \\ & \times \sum_{i=1}^2 (-1)^i \{ \exp[(-1)^i WZ] \operatorname{erfc}[(-1)^i W\sqrt{T} \\ & + Z/(2\sqrt{T})] \} \left. \right) dQ. \quad (22) \end{aligned}$$

To discuss the behavior of  $\Phi_C(X, Z, T)$ , let us assume  $Z=0$  for the sake of simplicity. Then the stationary variation in concentration induced by the photochemical reaction behaves as  $\Phi_C(X, Z=0, T=\infty) \sim \int_{-\infty}^{+\infty} \{f(Q) e^{-iQX} / [Q(Q+W)]\} dQ$ . Thus, the contribution of the  $Q=0$  mode (i.e., the background in the plane wave approximation) diverges. Considering the Gaussian shape of the pump waves instead of plane waves, this divergence at  $Q=0$  means that at late stage, the pumps mainly drive the variation in concentration. Consequently, the contrast of the modulation forced by the fringe pattern is progressively blurred by the contribution of the

$Q=0$  mode. This behavior is typical to a nonlocal process [44]. To go further on this analysis we solve Eq. (22) for  $Z=0$ . We obtain

$$\begin{aligned} \Phi_C(X, Z=0, T) = & \frac{K_{AB}P}{D_C} \left( \frac{1}{W^2} \left[ \frac{2}{\sqrt{\pi}} W\sqrt{T} - 1 \right. \right. \\ & \left. \left. + \exp(W^2T) \operatorname{erfc}(W\sqrt{T}) \right] \right. \\ & + \frac{\cos(Q_0X)}{W^2 - Q_0^2} \left\{ \frac{W}{Q_0} \operatorname{erf}(Q_0\sqrt{T}) - 1 \right. \\ & \left. \left. + \exp[(W^2 - Q_0^2)T] \operatorname{erfc}(W\sqrt{T}) \right\} \right). \end{aligned} \quad (23)$$

The first term of the right-hand side of Eq. (23) corresponds to the contribution of the  $Q=0$  mode. The time scale  $T_{Q=0} = 1/W^2$  drives its kinetics. The second term describes the dynamics of the forced modulation. It is characterized by the time scale  $T_{Q=Q_0} = 1/Q_0^2$ . Since typical fringe spacing is of the order of a few microns and manageable absorption of photosensitive mixtures smaller than  $1 \text{ m}^{-1}$ , we see that  $T_{Q=Q_0}/T_{Q=0} \ll 1$ . Thus, the early-stage variation in composition is totally driven by the fringes while the contribution of the pump waves starts to influence the dynamics at later time to finally dominate the full process.

### B. Photochemical deposition driven by two interfering beams and deposit growth rate

As for the single beam configuration described in Sec. IV, these variations in composition can monitor a periodic liquid/solid phase transition. When solubility of species  $C$  is reached, spatially modulated precipitation occurs. Since such deposits are usually used in optical systems as phase or amplitude gratings, the important feature here is the control over their thickness. As discussed above, a deposit is characterized by a normalized absorption  $W'$ , which is generally different from that of the solution ( $W$ ). Then, looking for axial growth, the exciting intensity in the liquid phase in the presence of a photodeposit becomes  $I(X, Z) = [P/(\pi a_0^2)] [1 + \cos(Q_0X)] e^{-W(Z-H)} e^{-W'H}$  for  $Z > H$ , instead of Eq. (19) used to determine the variation in species  $C$  before the optical quenching in composition. Moreover, Eq. (15) gives the temporal behavior of the deposit relief, where the concentration  $\Phi_C$  is calculated from Eqs. (20) and (21) with the appropriate boundary conditions: complete attenuation at infinity  $\Phi_C(X, Z \rightarrow \infty, T) = 0$  and solute adsorption  $\Phi_C(X, Z=H, T) = 0$  on the deposit. Reassembling these points, we find that the scaled height  $H_d$  of the modulated deposit is given by

$$\begin{aligned} H_d = & \frac{1}{W'} \ln \left[ 1 + \frac{K_{AB}W'P}{D_C} \int_0^T [F(T', Q=0) \right. \\ & \left. + \cos(Q_0X)F(T', Q=Q_0)] dT' \right]. \end{aligned} \quad (24)$$

As a result, the temporal behavior of the deposit height is

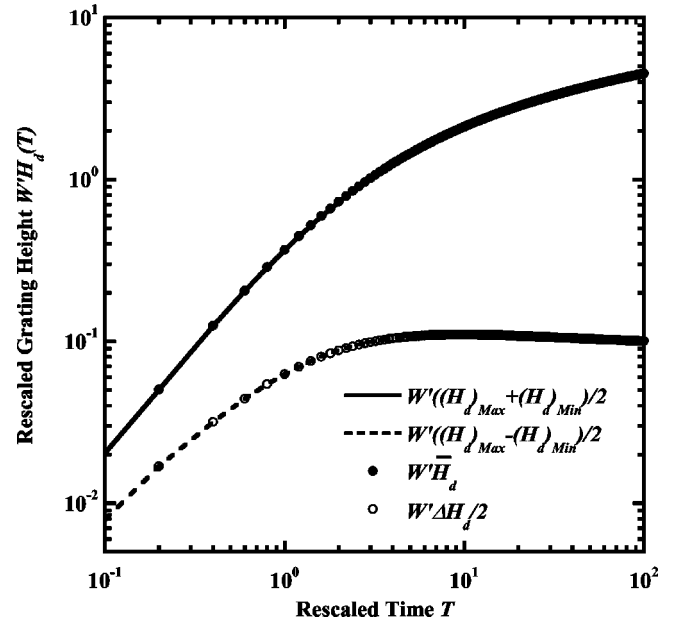


FIG. 8. Temporal behaviors of the mean deposit height  $W'[(H_d)_{Max} + (H_d)_{Min}]/2$  and the half amplitude of its modulation  $W'[(H_d)_{Max} - (H_d)_{Min}]/2$  forced by the  $Q=Q_0$  mode. For comparison, also presented are  $W'\bar{H}_d(T)$  and  $W'\Delta H_d(T)$  corresponding, respectively, to the  $Q=0$  and  $Q=Q_0$  modes in the approximation  $W'H_d(X, T) \approx W'\bar{H}_d(T) + [W'\Delta H_d(T)/2]\cos(Q_0X)$ . Note the difference in amplitude between these two contributions. The parameters used are  $Q_0=10$ ,  $W=1$ , and  $K_{AB}W'P/D_C=1$ .

described by a logarithmic variation of the sum of two contributions: the background corresponding to the pumps and represented by the  $Q=0$  mode, and the modulation driven by the forced  $Q=Q_0$  mode. Let us assume the typical values  $Q_0=10$  and  $W=1$ . As  $F(T, Q) \approx (2/\sqrt{\pi})\sqrt{T}$  does not depend

on  $Q$ , we see that the  $Q=0$  and the  $Q=Q_0$  modes contribute equally to the kinetics at the early stage of the deposition process. On the other hand, as  $F(T \rightarrow \infty, Q=Q_0)/F(T \rightarrow \infty, Q=0) = W/(W+Q_0)$ , we expect that the dynamics at late stage is monitored by the background contribution  $Q=0$ . These behaviors are illustrated in Fig. 8 that shows the temporal variations of the mean deposit height  $W'[(H_d)_{Max} + (H_d)_{Min}]/2$  and the half amplitude of its modulation  $W'[(H_d)_{Max} - (H_d)_{Min}]/2$ ; we state  $K_{AB}W'P/D_C=1$  for the sake of simplicity.

While Eq. (24) gives the general formula for the deposit height, its nonlinear behavior prevents any further analytical description of the resulting optical properties in terms of diffracted amplitudes. Indeed, when working with holographic gratings it is important to separate as much as possible the background to the modulation contribution because the former usually acts as an amplitude pedestal (its phase shift is constant) while the latter gives the phase shift required to characterize the diffraction properties. To do so we use the properties of the function  $F(T, Q)$ . Since  $F(T, Q) \approx (2/\sqrt{\pi})\sqrt{T} \ll 1$  at the early-stage growth and  $F(T, Q=Q_0) \ll F(T, Q=0)$  at later time, the influence of the nonlinear

$T \ll 1$   
 $\ll F(T, Q=0)$  at later time, the influence of the nonlinear

logarithmic behavior is in fact weak, and  $H_d$  can be decomposed as  $H_d(X, T) \approx \bar{H}_d(T) + [\Delta H_d(T)/2] \cos(Q_0 X)$ , where the contributions of the modes  $Q=0$  and  $Q=Q_0$  are

$$\begin{aligned} \bar{H}_d(T) &= \frac{1}{W'} \ln \left[ 1 + \frac{K_{AB} W' P}{D_C} \int_0^T F(T', Q=0) dT' \right], \\ \Delta H_d(T) &= \frac{2K_{AB} P}{D_C} \frac{\int_0^T F(T', Q=Q_0) dT'}{1 + \frac{K_{AB} W' P}{D_C} \int_0^T F(T', Q=0) dT'}. \end{aligned} \quad (25)$$

For comparison,  $\bar{H}_d(T)$  and  $\Delta H_d(T)$  are also represented in Fig. 8. It can be noticed that the explicit separation in spatial Fourier modes fairly well reproduces the general expectations. As a consequence, this very good approximation facilitates the dynamical interpretation of the resulting diffraction pattern and allows us to separately determine the kinetics of the pedestal and the modulation of the induced surface relief grating [45].

## VI. CONCLUSION

In the present paper we have theoretically investigated the kinetics of periodic surface patterning resulting from laser-induced photochemical deposition in liquid solutions. This study was undertaken in view of understanding the different steps involved in the optical excitation of photosensitive liquid mixtures to form surface relief gratings. Due to its technological significance in material science, particularly in patterning diffractive elements, and to the diversity in materials deposited, it is particularly appealing to build models that are system independent as much as possible. Therefore, one can avoid to continuously repeat the same tedious characterization when excitation or material is changed. Preliminary results needed a theoretical background to understand the different mechanisms involved and to investigate the resulting potentialities in material processing. To analyze the kinetics properties of the induced patterning, we started from the very beginning of the optical excitation process by describing the optical quenching mechanisms driven by a photochemical reaction. We derived the laser-induced photodeposit growth for different significant experimental configurations. Three main stages are involved in photochemical deposition. At first, a new species has to be generated by a photochemical reaction. We described this production by building a reaction/diffusion analysis in presence of light excitation. The important point concerning the evolution of the induced species is that production is intrinsically nonlocal due to light absorption within the medium. This means that the spatial distribution of the produced species does not follow exactly the electromagnetic field excitation; it is wider due to dissipation. Then, as soon as concentration reaches solubility, a deposit is heterogeneously nucleated on the substrate. We did not describe this second stage. Instead we focus our attention

on the third stage that consists in the photodeposit growth under illumination. Indeed, in this regime we reach deposit length scales that are particularly attractive for optical applications. Moreover, the deposition kinetics does not depend anymore on the substrate roughness and thus, as for the kinetics of phase transitions [36], one expect growth to be described by universal scaling behaviors. That was our main motivation in developing this study.

We have investigated this aspect in three distinct cases that represent the main classes of surface patterning used in applications. We first analyzed the most simplest case represented by the deposition of a patch (in fact a deposit with a spherical cap shape) under the excitation by a classical Gaussian laser wave. We have seen that its late-stage radial growth is characterized by different scaled laws depending on the ratio between the beam waist and the optical absorption length associated with the mixture; light absorption in the medium brings a second length scale that can compete with the beam size and, thus, modify the medium response to excitation. So, we extended coarsening theories, used for the description of the kinetics of first-order phase transitions at late stage, to laser-assisted photochemical deposition. We explain the origin of these scaling behaviors according to the general picture of coarsening phenomena driven by solute diffusion and adsorption. Since a spherical cap growth model obviously fails for thick deposits (spherical shapes are generally sustained by surface tension), we also described the height growth to provide a description of the deposit morphology as complete as possible. We recover an Elovich' formulation of the height growth dynamics that was used to analyze experimental data [41]. We then extended the model to dynamic line writing by photochemical deposition. This aspect is also important because lines are often deposited to repair circuits and build electric contacts [42,43], for instance. The scanning velocity appears as a new variable to dynamically control at the same time the wideness and the thickness of the deposited line. Finally, using two interfering pump beams, we describe the dynamic building of a photodeposited holographic grating. Strictly speaking, it does not follow exactly the electromagnetic field distribution because the nonlocal response of the medium has an important contribution around the  $q=0$  Fourier mode. However, as far as the evolving time is not too large, the background contribution, represented by the  $q=0$  mode, can be decoupled from the modulation driven by the forced mode  $q=q_0$ . This separation is of particular interest when dealing with dynamic control of amplitude and phase shifts of diffracted waves associated to periodic patterning. In terms of phase shift, the pedestal associated with the  $q=0$  mode is constant in space while the beam attenuation associated to the modulation is clearly negligible compared to that of the background.

As a conclusion, the present work shows how the dynamics of periodic patterning by photochemical deposition can be theoretically investigated. A major point is the emergence of scaling regimes that can be used to predict the properties, as well as the optical performances, of the induced patterning. Due to the crucial role played by photodeposition and its control in numerous practical applications (surface patterning, lithography, or holography, for instance), this universal

picture may represent a first step toward a unified description of the processes involved. That is why the confrontation of predictions to experiment is explored in a companion paper using the photoreduction of chromates by continuous Ar<sup>+</sup>

laser waves in liquid solutions. The experimental data we obtain show excellent agreement with our model, giving valuable insights into the underlined physics for the design of photodeposited holographic elements.

- 
- [1] Y. Xia, J. A. Rogers, K. E. Paul, and G. M. Whitesides, *Chem. Rev.* (Washington, D.C.) **99**, 1823 (1999).
- [2] P. Rai-Choudhury, *Handbook of Microlithography, Micromachining, and Microfabrication* (SPIE Optical Engineering Press, Bellingham, 1997), Vol. 1.
- [3] S. Hong, J. Zhu, and C. A. Mirkin, *Science* **286**, 523 (1999); S. Hong and C. A. Mirkin, *ibid.* **288**, 1808 (2000).
- [4] M. M. Burns, J. M. Fournier, and J. A. Golovchenko, *Science* **249**, 749 (1990).
- [5] Y. Xia, D. Qin, and Y. Yin, *Curr. Opin. Colloid Interface Sci.* **6**, 54 (2001).
- [6] S. D. Wu and E. N. Glytsis, *J. Opt. Soc. Am. B* **20**, 1177 (2003).
- [7] R. L. Sutherland, *J. Opt. Soc. Am. B* **19**, 2995 (2002); R. L. Sutherland, L. V. Natarajan, V. P. Tondiglia, S. Chandra, C. K. Shepherd, D. M. Brandelik, and S. A. Siwecki, *ibid.* **19**, 3004 (2002).
- [8] C. Moi and D. W. M. Marr, *Langmuir* **15**, 8565 (1999).
- [9] G. Krausch, *Mater. Sci. Eng., R.* **R14**, 1 (1995); S. Puri and H. L. Frisch, *J. Phys.: Condens. Matter* **9**, 2109 (1997).
- [10] J. Y. Kim and P. Palfy-Muhoray, *Mol. Cryst. Liq. Cryst.* **203**, 93 (1991).
- [11] A. Golemme, G. Arabia, and G. Chidichimo, *Mol. Cryst. Liq. Cryst. Sci. Technol., Sect. A* **243**, 185 (1994).
- [12] S. Buil, E. Hugonnot, and J. P. Delville, *Phys. Rev. E* **63**, 041504 (2001).
- [13] J. Y. Kim, C. H. Cho, P. Palfy-Muhoray, M. Mustafa, and T. Kyu, *Phys. Rev. Lett.* **71**, 2232 (1993).
- [14] M. Bhattacharya, D. G. Vlachos, and M. Tsapatsis, *Appl. Phys. Lett.* **82**, 3357 (2003).
- [15] H. K. Henisch, *Crystal in Gels and Liesegang Rings* (Cambridge University Press, Cambridge, 1988).
- [16] D. Bäuerle, *Laser Processing and Chemistry* (Springer-Verlag, Berlin, 1996).
- [17] G. A. Shafeev, *Thin Solid Films* **218**, 187 (1992).
- [18] A. Peled, *Lasers Eng.* **6**, 41 (1997).
- [19] V. Weiss, A. A. Friesem, and A. Peled, *J. Imaging Sci. Technol.* **41**, 355 (1997).
- [20] K. Kordás, L. Nánai, K. Bali, K. Stépan, R. Vajtai, T. F. George, and S. Leppävuori, *Appl. Surf. Sci.* **168**, 66 (2000); K. Kordás, K. Bali, S. Leppävuori, A. Uusimäki, and L. Nánai, *ibid.* **154/155**, 399 (2000).
- [21] M. Ichimura, N. Sato, A. Nakamura, K. Takeuchi, and E. Arai, *Phys. Status Solidi A* **193**, 132 (2002).
- [22] E. Hugonnot, X. Müller, and J. P. Delville, *J. Appl. Phys.* **92**, 5520 (2002).
- [23] A. Peled, Y. Dror, I. Baal-Zedaka, A. Porat, N. Mirchin, and I. Lapsker, *Synth. Met.* **115**, 167 (2000).
- [24] A. Peled, V. Baranauskas, C. Rodrigues, D. Art-Weisman, L. Grantman, and A. A. Friesem, *J. Appl. Phys.* **77**, 6208 (1995).
- [25] A. Lachish-Zalait, D. Zbaida, E. Klein, and M. Elbaum, *Adv. Funct. Mater.* **11**, 218 (2001).
- [26] V. Weiss, A. Peled, and A. A. Friesem, *Appl. Opt.* **33**, 4988 (1994).
- [27] I. Baal-Zedaka, S. Hava, N. Mirchin, R. Margolin, M. Zagon, I. Lapsker, J. Azoulay, and A. Peled, *Appl. Surf. Sci.* **208/209**, 226 (2003).
- [28] E. Hugonnot, A. Carles, M. H. Delville, P. Panizza, and J. P. Delville, *Langmuir* **19**, 226 (2003).
- [29] E. Hugonnot, A. Popescu, S. Kadi-Hanifi, and J. P. Delville, *Phys. Rev. E* **69**, 051606 (2004).
- [30] A. J. Bray, *Adv. Phys.* **43**, 357 (1994).
- [31] A. Yariv, *Quantum Electronics* (Wiley, New York, 1989).
- [32] W. H. Lowdermilk and N. Bloembergen, *Phys. Rev. A* **5**, 1423 (1972).
- [33] M. Lax, *J. Appl. Phys.* **48**, 3919 (1977).
- [34] E. Abraham and J. M. Halley, *Appl. Phys. A: Solids Surf.* **A42**, 279 (1987).
- [35] S. Buil, J. P. Delville, and A. Ducasse, *Phys. Rev. Lett.* **82**, 1895 (1999).
- [36] J. D. Gunton, M. San Miguel, and P. S. Sahni, in *Phase Transitions and Critical Phenomena*, edited by C. Domb and J. L. Lebowitz (Academic, New York, 1983), Vol. 8, p. 269.
- [37] T. Vicsek, *Fractal Growth Phenomena* (World Scientific, Singapore, 1992).
- [38] J. P. Delville, C. Lalaude, S. Buil, and A. Ducasse, *Phys. Rev. E* **59**, 5804 (1999).
- [39] S. R. Corriel and R. L. Parker, *J. Appl. Phys.* **36**, 632 (1965).
- [40] D. K. Yi, M. J. Kim, and D. Y. Kim, *Langmuir* **18**, 2019 (2002).
- [41] A. Peled, A. A. Friesem, and K. Vinokur, *Thin Solid Films* **218**, 201 (1992).
- [42] M. Hanabusa, *Thin Solid Films* **218**, 144 (1992).
- [43] T. H. Baum and P. B. Comita, *Thin Solid Films* **218**, 80 (1992).
- [44] E. Freysz, E. Laffon, J. P. Delville, and A. Ducasse, *Phys. Rev. E* **49**, 2141 (1994).
- [45] E. Hugonnot and J. P. Delville, *Appl. Phys. Lett.* **80**, 1523 (2002).